449

A stochastic kinetic energy backscatter algorithm for use in ensemble prediction systems

Glenn Shutts

Research Department

Abstract

Physical justification is provided for the use of kinetic energy backscatter in forecast models, particularly in respect of ensemble prediction system. The rate of energy backscatter to scales near the truncation limit is controlled by a total energy dissipation function involving contributions from numerical diffusion, mountain drag and deep convection. A cellular automaton is used to generate evolving patterns that, together with the dissipation function, define a streamfunction forcing field. Each member of the ECMWF ensemble forecast system is perturbed by a different realization of this backscatter forcing and the resulting increase in ensemble spread, if not excessive, has a beneficial impact on probabilistic measures of forecast skill. The input of small-scale kinetic energy by the backscatter algorithm also helps to correct a known problem with the energy spectrum in the ECMWF model – the absence of the observed $-5/3$ spectral slope in the mesoscales.

1. Introduction

Forecast error is deemed to be the result of imperfections in both the initial atmospheric state and in imperfections of numerical weather forecast model formulation. Model error is associated with basic design choices that define the adiabatic framework of the model (e.g. spectral, gridpoint, finite element; vertical coordinate system; the advection scheme and its related truncation error) and a component due to errors in physical parametrization. Ensemble prediction systems exploit the sensitivity of numerical weather forecasts to initial conditions and carry out many forecasts from slightly different initial atmospheric states. In order to address forecast error resulting from model imperfection, the ECMWF Ensemble Prediction System (EPS) attempts to account for the uncertainty in parametrized fluxes associated with the statistical nature of the sub-gridscale processes they represent (Buizza et al, 1999). In this approach the total sub-gridscale parametrization tendency at all points within predefined latitude/longitude boxes is multiplied by a number selected randomly, with uniform probability, from the range 0.5 to 1.5. A uniform latitude/longitude grid with 10-degree resolution is used operationally to define these boxes and the numbers are updated every six hours.

The random numbers used in the ECMWF EPS have crude spatial and temporal correlation through their constancy within the boxes and within six-hour time intervals. In middle latitudes this spatial correlation scale is comparable with the Rossby deformation radius and the time scale is about twice the Coriolis time scale $(1/f)$ implying that the resulting stochastic flow perturbations will project well onto the balanced part of the flow. Smaller correlation scales tend to generate high frequency gravity waves whose impact on weather system evolution is only slight. Perturbations in the parametrization increments generated by the scheme are meant to represent statistical fluctuations about the ensemble-mean value. In the case of convective parametrization one could relate these fluctuations to the low convective cloud population density (with respect to model resolution) so that the number of clouds within a gridbox fluctuates substantially. For mountain flow drag parametrization (gravity wave drag and flow blocking contributions) the origin of statistical fluctuation could plausibly come from nonlinearity in the flow dynamics (e.g. drag fluctuations due to eddy shedding in the low mountain Froude number regime).

Apart from these early attempts to improve the skill of ensemble forecasting, considerable interest in the use of stochastic representations of atmospheric processes has developed recently and this trend seems set to continue. In the context of deep convection parametrization in the tropical atmosphere, Lin and Neelin (2000, 2002) have experimented with different strategies to account for higher moment fluctuations in

vertical fluxes and precipitation rate. Since deep convection plays a dominant role in tropical circulation - both with respect to the mean climatology and low frequency oscillations - it is important to establish whether the effect of these statistical fluctuations in convection are important. They found that although the near-grid scale dynamical response of the model they used made it difficult to achieve the desired statistical behaviour, the impact of stochastic convection parametrization on low frequency tropical wind variability was substantial.

Williams et al (2004) have shown how small amplitude stochastic perturbations representing the effects of inertia-gravity waves can influence wavenumber selection in a model of a rotating annulus. They directly forced the potential vorticity field of a two-layer quasi-geostrophic model using suitably scaled random numbers, though without spatial or temporal correlations. The effect of the perturbations was only large in certain favourable regions of parameter space close to wavenumber transition boundaries. Their numerical simulations complement and support the findings of rotating annulus experiments in which spontaneously generated inertia-gravity waves assist wavenumber transition (Williams, 2003).

Outside of model parametrization schemes, truncation error in the computation of advection reduces the variance in model fields. In practice, a level of horizontal diffusion is required to maintain smoothness at the gridscale, dependent on the diffusive properties of the advection scheme in use. For instance in the semi-Lagrangian advection scheme, interpolation of field values to the departure point has a net smoothing effect with cubic interpolation behaving like bi-harmonic diffusion (McCaplin, 1988). Although observational estimation of the magnitude of turbulent energy dissipation is notoriously difficult (Kennedy and Shapiro, 1975; Chapman and Browning, 2001) it seems likely that these model diffusive effects consume kinetic and available potential energy at an unrealistically excessive rate. For instance horizontal diffusion and interpolation error limit the frontogenesis process in numerical weather prediction (NWP) models but are unlikely to be a satisfactory representation of the true discontinuity-limiting physical process e.g. Kelvin-Helmholtz instability.

In the context of Large Eddy Simulation (LES) of the turbulent boundary layer Mason and Thomson (1992) demonstrated the positive impact of near-gridscale stochastic momentum forcing scaled with the local kinetic energy dissipation rate. They reasoned that the viscous drain of energy by the Smagorinsky-Lilly formulation of eddy viscosity reduces the effectiveness of poorly resolved eddies in transporting momentum to the surface. In order to match the momentum flux by larger-scale eddies, the explicitly resolved flow must sustain stronger near-surface mean shear and the simulated flow departs significantly from the observed logarithmic variation with height. Their *stochastic backscatter* formulation excites energy at scales close to the model truncation limit and represents a flow of energy from sub-grid scales to explicitly resolved scales. In simulations with stochastic backscatter, vertical profiles of horizontally averaged flow more nearly approximate the textbook log-law.

It is argued here that the energy sink implied by numerical advection error and horizontal diffusion in NWP models is unrealistically large and that a suitably contrived near-grid scale stochastic forcing function could be used to inject energy back into the model in a similar manner to the stochastic backscatter approach of Mason and Thomson. However in the numerical weather prediction setting there are several additional sub-grid scale kinetic energy sources to be considered such as that associated with the rate of working of the buoyancy force in cumulus convection.

In this paper it is shown how the computation of these kinetic energy sources in the ECMWF forecast model can be combined with a cellular automaton (CA) pattern generator to define a stochastic backscatter algorithm entitled CASBS - Cellular Automaton Stochastic Backscatter Scheme. The impact of CASBS on ensemble forecasts is assessed in relation to the current operational 'stochastic physics' scheme using standard probabilistic measures of forecast skill.

The outline of the paper is as follows. The physical motivation behind CASBS is described in section 2 and its implementation in the ECMWF model, together with a discussion of the cellular automaton, is provided in section 3. In section 4 the character of the dissipation and backscatter forcing fields is examined and the impact of CASBS on forecast skill in two sets of 10 forecasts is described, with concluding remarks in section 5.

2.   Physical basis for energy backscatter

2.1   Energy backscatter estimates

Since observational estimation of atmospheric energy dissipation rates is subject to considerable uncertainty the task of estimating local upscale energy transfer rates will also be prone to much error. The intensity of turbulent kinetic energy dissipation will naturally vary by orders of magnitude from place to place given its cubic dependence on velocity and so representivity will always be a problem - even if measurement techniques were accurate. In spite of these problems the global-mean energy dissipation rate associated with vertical mixing can be assessed from numerical weather prediction models and is probably accurate to within a factor of 2. In the ECMWF model the global-mean energy dissipation rate due to parametrized vertical mixing is ~ 2 Wm^{-2}. If the mean boundary layer depth is taken to be about 1 km and air density ~ 1 $kg\ m^{-3}$ then the mean energy dissipation rate per unit mass (ε) is ~ $2 \times 10^{-3}\ m^2 s^{-3}$. Suppose that the dissipation rate due to other local sources in the free atmosphere (e.g. due to gravity wave breaking over a broad mountain range) is comparable in size. If one tenth of this is transferred upscale rather than dissipated as heat, the associated energy backscatter rate (ε_b is ~ $2 \times 10^{-4}\ m^2 s^{-3}$) implies an energy tendency of about 20 $m^2 s^{-2}/day$ equivalent to a local flow acceleration of ~ 4 or 5 ms^{-1} per day. This force (per unit mass) is quite small relative to a typical Coriolis force magnitude of $10^{-3}\ ms^{-2}$ or roughly 100 ms^{-1} per day (taking the Coriolis parameter $f = 10^{-4}\ s^{-1}$ and wind speed $V = 10\ ms^{-1}$). Since the Lagrangian flow acceleration of air parcels is about one tenth of this, it is likely that the above backscatter forcing should have a tangible impact on forecast evolution, particularly in regions of intense dissipation.

Having demonstrated the plausible influence of kinetic energy backscatter on forecast model evolution we will now consider in detail the various physical and numerical sources of dissipation that will contribute to an estimate of the total energy dissipation rate.

2.2   Horizontal diffusion and interpolation error

The inclusion of horizontal diffusion in NWP or climate models is rarely justified on physical grounds and in any case many types of advection scheme are inherently diffusive. Diffusion acts to maintain smooth fields at the gridscale preventing noise associated with frontal discontinuity formation, topographic fields and convection parametrization. Numerical advection schemes such as the semi-Lagrangian technique may be used without the need for horizontal diffusion since interpolation itself acts to smooth fields. In practice, best results are obtained with a judicious choice of horizontal diffusion that matches the inherent diffusivity of the

advection scheme. This combined diffusive effect of horizontal diffusion and interpolation error on the energy will be referred to as 'numerical energy dissipation'. All other contributions to the energy dissipation arise from physical parametrization terms in the model equations. The aim of this section is to provide some support for the idea that numerical energy dissipation is excessive in NWP models.

Direct estimates of the energy dissipation due to interpolation error in the forecast model are not presently available but some published energy diagnostics from other models help to assess the total numerical dissipation. Côte and Staniforth (1988) and Ritchie (1988) carried out 20-day integrations of the shallow water equations with different forms of the semi-Lagrangian advection algorithm and find a 3% total energy loss over the integration period. The conservation properties of these semi-Lagrangian schemes are shown to be similar to, or somewhat better than, those in a spectral model of equivalent resolution that uses α ∇^4 hyperviscosity. The spectral model conserves energy in the absence of numerical smoothing and so the hyperviscosity leads to similar energy losses as interpolation error in the semi-Lagrangian model. It will be assumed therefore that the energy dissipation rates found in spectral models with hyperviscosity are representative of the numerical energy dissipation rates in semi-Lagrangian models. However the levels of dissipation found in these shallow water model simulations are unlikely to be realistic given that the equations do not support frontogenesis and have no vertical wind shear.

The idealized baroclinic wave life cycle experiments of Simmons and Hoskins (1978) provide some measure of the likely levels of dissipation in an NWP context. Their Figure 5 shows a time series plot of globally averaged energy conversions and dissipation due to internal diffusion over the course of a baroclinic wave development and its subsequent decay. Internal diffusion is represented by a ∇^4 hyperviscosity term acting on vorticity, divergence and temperature and in the mature phase of the baroclinic wave this results in a peak energy dissipation rate of about $0.8 Wm^{-2}$. No surface boundary layer parametrization was included.

MacVean (1983) looked at the effect of differing levels of scale selectivity in hyperdiffusion at different horizontal resolutions. He found that the total energy dissipation over the course of a baroclinic life cycle appears to converge to a value that represents about 45% of the total conversion of potential energy to kinetic energy as the scale selectivity is increased. As speculated by Simmons and Hoskins (1978) this suggests that the amount of energy dissipated is set by large-scale flow information in the initial state rather than the precise form of the diffusion term provided that the baroclinic wave and associated fronts are sufficiently well resolved. The total energy dissipation in MacVean's simulations over the whole baroclinic life cycle amounts to about $2 \times 10^5 Jm^{-2}$ which over a time scale of 10 days (typical of the active phase) is equivalent to ~0.2 Wm^{-2}. A visual estimate of the mean dissipation rate in the Simmons/Hoskins life cycle experiment (based on their figure 5) suggests a similar value.

Stephenson (1994) examined the sensitivity of a spectral general circulation model to changes in the hyperdiffusivity and found a large impact on certain energy conversion terms. He also showed an energy box diagram derived from ECMWF analyses for the winter 1991/92 in which the implied net dissipation of kinetic energy is 1.53 Wm^{-2}. Unfortunately the contribution of horizontal smoothing to this total dissipation value was not presented and boundary layer friction is likely to be the dominant contribution.

From a different viewpoint Blumen (1990) used a semi-geostrophic model of frontogenesis to examine the development of fronts in the presence of momentum diffusion. The collapse of the near-surface frontal width

to zero is prevented by diffusion, and kinetic energy is dissipated in the resulting mixing zone. Energy dissipation rates as large as 50 - 250 Wm^{-2} are found in the model though Blumen warns of the inherent uncertainty in the value. In spite of these huge values (nearly two orders of magnitude greater than a nominal boundary dissipation value) he estimates that the global-mean energy dissipation due to horizontal mixing in fronts is less than the global-mean boundary layer dissipation. Blumen's model is likely to be representative of the balance of physical processes that occur in NWP model fronts where numerical diffusion limits scale collapse to a discontinuity. The convergence of the energy dissipation rate found by MacVean (1983) with increasing scale selectivity is relevant to mathematical solutions in which horizontal hyperviscosity plays a key role. However Cullen and Purser (1983) showed, in an extended Lagrangian semi-geostrophic model, that it is not necessary to invoke viscosity after the point of frontal collapse. Inviscid solutions could still be constructed but now with a discontinuity surface protruding from the boundary. Whilst one would not want to claim that such solutions are accurate models of real frontogenesis they emphasize the possibility that frontal collapse can proceed down to very small horizontal scales (e.g. comparable with the depth of the boundary layer) without the need to invoke vigorous horizontal mixing.

Observational measurement of frontal dissipation is difficult to make although using aircraft data Kennedy and Shapiro (1975) estimate energy dissipation rates of $\sim 2\times10^{-2}$ m^2s^{-3} (equivalent to ~ 75 Wm^{-2} over the dissipating layer) in an upper front. There is however some doubt as to the representivity of such high values. Chapman and Browning (2001) carried out a systematic study of the Doppler spectrum width from high-resolution radar and estimate a spatially averaged frontal energy dissipation rate of $\sim 10^{-3}$ m^2s^{-3} - some 20 times smaller than the Kennedy and Shapiro estimate. As a mass-weighted vertical integral this corresponds to a few Watts per square metre i.e. similar to a typical frictional boundary layer dissipation rate and far smaller than Blumen's model estimate. The energy dissipation occurred in shallow-sloping layers of high turbulence intensity embedded within the frontal zone consistent with vertical mixing in high shear zones. Horizontal mixing in regions of high lateral shear, as represented in NWP models, is not a very convincing physical model of the process that opposes frontal collapse. One could speculate that the energy dissipation rates found in Blumen's model and MacVean's sensitivity study are too high and characteristic of an unphysical description of frontogenesis in which horizontal smoothing or mixing dominate over the familiar vertical mixing in low Richardson number shear layers.

In the context of stochastic backscatter we imagine that a substantial part of the kinetic energy lost through horizontal diffusion or semi-Lagrangian interpolation error is not dissipated by turbulence but effectively remains as a hidden sub-grid scale contribution. Horizontal diffusion in a forecast model is regarded as one of many processes that contribute to the sub-grid scale kinetic energy of which a certain fraction is 'backscattered' into the partially resolved scales of an NWP model.

2.3 Mountain and gravity wave drag

In most current NWP models the effect of sub-grid scale orography is parametrized through a low-level 'flow blocking' drag force and a term describing the effect of stationary gravity waves. The force opposes the local flow and so appears in the energy equation as a sink of kinetic energy. From a numerical standpoint the dissipation of energy implied by this type of parametrization may locally be very large and in the ECMWF forecast model values as high as 200 Wm^{-2} are common over the mountains of the Himalayas and South American Andes. As with frontal dissipation one might question whether or not this dissipation rate reflects real turbulent energy dissipation and conversion to heat or whether a large fraction goes into sub-grid

scale motion and then back upscale. The drag force associated with flow past mountainous islands is associated with pressure differences across orographic features of differing scales. The small-scale features generate three-dimensional turbulence whereas the island-scale orography generates quasi-2D eddies (the familiar von Karman vortices seen in downstream cloud formations). These quasi-two-dimensional motions in a stratified fluid are subject to Fjortoft's theorem (Fjortoft, 1953), which requires that spreading of energy in wavenumber space is accompanied by more energy flowing upscale than downscale due to the enstrophy conservation constraint. Consequently it is difficult for such motions to dissipate energy and the eddies shed from mountains may be absorbed into the larger scale flow or coalesce with each other. Most of the three-dimensional turbulent energy is dissipated at the molecular level as heat and only a small fraction is available to backscatter onto the near-grid scale of NWP models.

Another part of the total mountain drag force is due to radiating internal gravity waves that transmit their drag contribution to regions remote from the mountain (e.g. the stratosphere). Sub-grid scale gravity wave breaking generates potential vorticity anomalies as well as three-dimensional turbulence and the former may contribute to an upscale transfer of energy in the same manner as quasi-2D vortices shed from mountains. The efficiency of energy backscatter due to these mountain-related processes is not known and it will be necessary to appeal to 2D turbulence theory to make some plausible estimates.

2.4   Deep convection

Buoyancy forces in convective clouds generate kinetic energy on a range of scales that extend from the 1 km scale of boundary layer cumulus out to the 500 km scale (or more) of mesoscale convective anvils. Most convective parametrization schemes do not explicitly address the fate of the kinetic energy released by buoyancy focusing instead on the thermodynamic impact of a large population of sub-gridscale clouds as a function of the convective mass flux. In the context of shallow convection in boundary layers, energy in the convective circulations will dissipate as three-dimensional turbulence, radiate as gravity waves out of the boundary or be converted to potential energy. From a thermodynamic viewpoint the warming that results from kinetic energy dissipation is negligible compared with that due to surface energy fluxes and is often neglected in parametrization schemes.

Lilly (1983) put forward the view that a small fraction of the turbulence generated in convective anvils might participate in an upscale energy cascade consistent with the observed $k^{-5/3}$ spectrum at horizontal wavelengths less than about 400 km (Nastrom and Gage, 1985). He argued that only a few percent of the total energy dissipation rate would be required to account for the shallow spectral slope at small to mesoscales. Vallis et al (1997) carried out simulations with a cloud-resolving model with a view to quantifying the upscale influence of deep convection and examine the effect of background rotation. They found an energy spectrum at statistical equilibrium not dissimilar to the $k^{-5/3}$ power law though the upscale energy flux was rather weak implying an energy source for wavelengths between 60 and 300 km of ~ 0.1 $m^2 s^{-2}$ per day or ~ 10^{-6} $m^2 s^{-3}$. The character of the convection simulated by Vallis et al (1997) is reminiscent of that found in cold cyclonic airstreams over the sea in winter i.e. organized into cells and lines with about 30 to 60 km spacing.

The efficiency of upscale energy transport is substantially greater for continental mesoscale convective systems where large amounts of mass are convected into the upper troposphere during the lifetime of the storm. Under these conditions Shutts and Gray (1994) showed that as much as 30% of the kinetic energy released may be trapped in balanced flows with distinctive potential vorticity features. In the following

section, it will be shown how the rate of export of kinetic energy to the cloud environment can be estimated in the ECMWF convective parametrization scheme (Tiedtke, 1989).

3.   Cellular Automaton Stochastic Backscatter Scheme (CASBS)

3.1   Background

The stochastic backscatter scheme of Mason and Thomson (1992) creates a pattern of near-grid scale forcing by defining a three-dimensional vector potential from random number triplets at each gridpoint scaled with the square-root of the 'energy drain' i.e. rate of energy loss due to eddy viscosity. The components of the vector potential corresponding to each random number are smoothed with a 1-2-1 filter and a momentum source is defined from the curl of the resulting vector field thereby ensuring a non-divergent forcing function. If the energy drain were to be spatially uniform, the smoothed field of random numbers would dictate the pattern of momentum forcing.

It was decided at a fairly early stage of this work to use a cellular automaton to generate spatially and temporally coherent patterns of forcing following the suggestion of Palmer (1997). In his view the CA would be probabilistic to the extent that the probability of cell birth and survival would depend on the number of living nearest neighbours and some forecast model parameter. For instance, he envisaged a CA that would mimic convective cloud clustering on a scale that would be functionally dependent on the local value of convective available potential energy. In contrast, the CA used here is independent of the forecast model i.e. it is simply a pattern generator. It does however have the potential to be coupled to the model fields though at this stage there is some merit in minimizing complexity wherever possible.

Ideally it would be desirable for the stochastic backscatter scheme to introduce balanced potential vorticity perturbations into the near-grid scale flow to minimize the production of gravity waves. As a compromise it is expedient to introduce pure vorticity perturbations into the model flow and tolerant some geostrophic adjustment. By analogy with LES stochastic backscatter, the CA pattern (suitably scaled with the square root of the dissipation rate) is taken to be proportional to a streamfunction forcing.

3.2   Pattern generation using a cellular automaton

A home-grown CA is used here to generate a complex evolving scalar field whose characteristic spatial and temporal scales are similar to those of the atmospheric mesoscale. This scalar field is treated as a streamfunction or velocity potential tendency for the purposes of calculating wind increments. For the T159 forecasts described here the CA is implemented on a 0.5-degree latitude/longitude grid and cell values are averaged onto a 2-degree grid for presentation to the model's reduced Gaussian grid. The 2-degree grid is referred to as the *intermediate CA grid* and is used to coarse-grain the pattern information in the CA grid so as to be compatible with near-grid scale of the forecast model.

The CA can be viewed as an extension to the well-known family of cellular automata called 'Generations' which add cell history to the original 'Game of Life' rules (Gardener, 1970). As a very simple illustration of how a CA works consider the cell array depicted in Figure 1. Here, each cell may be alive (red) or dead (white) and the state of the cells at the next step is governed by rules that involve their eight neighbours (referred to as the *neighbourhood*). A living cell will survive to the next step if it has either 2 or 3 living neighbours and a dead cell will remain dead unless it has exactly three living neighbours. Although the

change in pattern for this example is unremarkable, complex and interesting pattern evolution is readily found for quite simple survival and birth rules (Wolfram, 2002).
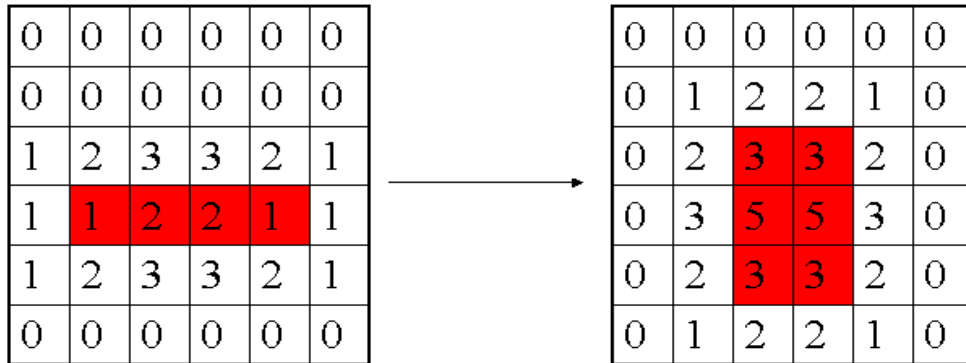

Figure 1 A simple cellular automaton in which cells are either alive (red) or dead (white). The two CA states show a transition based on the survival condition: 2 or 3 living nearest neighbours and the birth condition; 3 living neighbours. The numbers within boxes indicate the number of living nearest neighbours for that cell.

The CA developed here for use in stochastic physics schemes was selected for its similarity to the pattern evolution seen in certain fields in cloud-resolving model simulations (e.g. boundary layer temperature beneath a field of deep convective clouds). In it, each new cell has a prescribed number of lives (N_L) and is subject to the following birth and survival rules which count only living cells in the neighbourhood that have not yet lost a life (referred to here as 'fertile cells'). Cell survival requires exactly 3,4 or 5 fertile cells in the neighbourhood and the birth of a new cell requires 2 or 3 fertile cells in the neighbourhood. Non-fertile cells do not participate in the neighbourhood count and limit the space available for cell birth. Each time a cell fails the survival test the number of lives remaining (N_L) is decremented by 1 until reaching zero whereupon the cell is regarded as dead. The parameter N_L is treated as a constant here and set to the value of 32. It controls the spatial scale and the temporal properties of the CA patterns through the values of $N_L \Delta x$ and $N_L \Delta \tau$ respectively where Δx is the CA box size and $\Delta \tau$ is the time interval between successive CA states.

The CA is started by randomly seeding the grid with new cells and is advanced by 2000 steps to 'spin-up' the pattern. Figure 2(a) shows a graphical depiction of the integer array that defines a particular CA state. A scalar function Ψ_j is then defined by:

- coarse-graining the integer CA values to the intermediate CA grid
- smoothing with a 1-2-1 filter
- subtracting the resulting domain average so that Ψ_j has zero mean
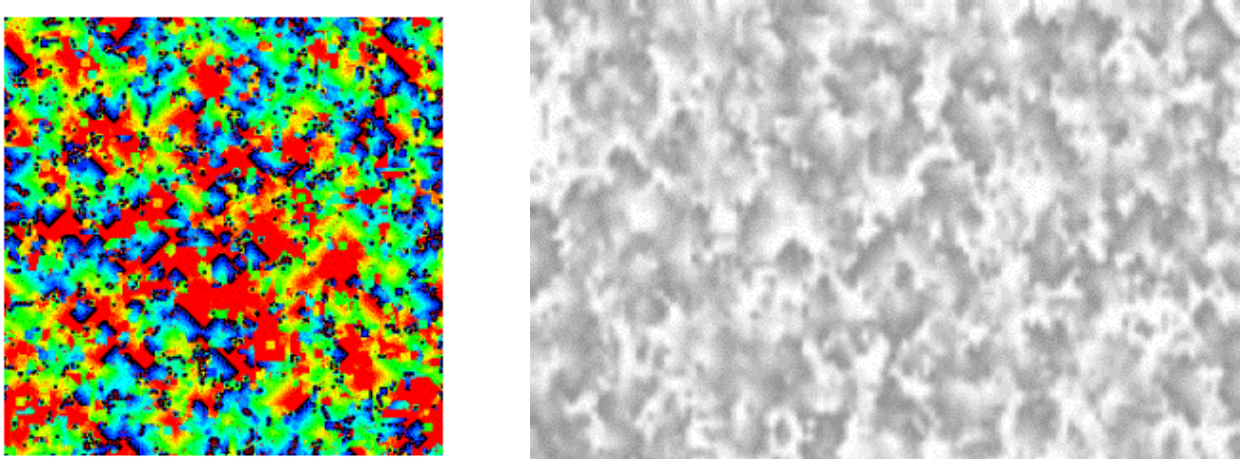
where the index *j* labels a model gridpoint.

Figure 2 (a) A colour-coded depiction of CA state based on cells that have 32 lives (see text for rule set). (b) an example of a 'weighting function' derived from the CA by coarse-graining, scaling and normalizing the integer-valued CA field

3.3   Implementation details

A streamfunction forcing field is define from the product of Ψ and the square root of a spatially-smoothed form of the *total energy dissipation rate* ($\hat{D}$) computed by summing contributions from the processes outlined in the previous section. Because the computed energy dissipation rate is a noisy field at the near-grid scale (reflecting the character of the physical parametrization increments) , it is spectrally-smoothed by multiplying the spherical harmonic coefficients by the function *S(n)* given by:

$$S(n) = \begin{cases} 1 & n < n_f \\ \exp\left(-3\dfrac{n(n+1) - n_f(n_f+1)}{n_c(n_c+1) - n_f(n_f+1)}\right) & n_f < n < n_c \\ 0 & n > n_c \end{cases} \tag{1}$$

where the values $n_f = 30$ and $n_c = 40$ are used here. The smoothing of the dissipation rate field may be regarded as a crude device for obtaining a local ensemble-average dissipation rate field. At an obvious practical level, the computed dissipation rate in a region of active convection like the tropical west Pacific looks quite spotty and whilst a part of this could be real (e.g. linked to island convection) a substantial fraction will be associated with numerical noise. The backscatter forcing function is defined by the following equation for the streamfunction forcing function F_ψ

$$F_\psi = \frac{1}{2}\alpha \cdot \Delta s \;\; \Psi(\lambda,\phi)\sqrt{\Delta\tau \cdot \hat{D}} / \Delta\tau \tag{2}$$

where $\Delta\tau$ is the time step between successive CA states, Δs is a nominal CA gridlength and α is a non-dimensional parameter that determines the backscatter fraction i.e. the fraction of the compute energy dissipation rate that is forced back into the near-grid scales. Note that the product $\Delta\tau \cdot \hat{D}$ represents the increase in sub-grid scale kinetic energy during a single CA time step and so its square root is a characteristic sub-grid wind speed fluctuation. The unsmoothed dissipation rate D is made up of contributions from numerical sources (D_N), mountain/ gravity wave drag (D_{GW}) and deep convection (D_C). Since horizontal diffusion is applied in spectral space, D_N is computed by transforming the spectral vorticity and divergence

increments into increments of the wind components u and v on the reduced Gaussian grid of the forecast model *and* multiplying by their corresponding local wind components. Summing these component contributions gives the kinetic energy change in the resolved flow, which may be positive or negative.

The ratio of the energy backscatter rate to the dissipation rate can be related to the constant α by the following argument. In Cartesian geometry $\Psi \to \Psi(x, y)$ and differentiating equation (2) with respect to x assuming that $\hat{D}$ is constant gives:

$$F_v = \frac{\partial F_\Psi}{\partial x} = \frac{1}{2}\alpha\,\Delta s \frac{\partial \Psi}{\partial x}\sqrt{\Delta \tau \cdot \hat{D}}\,/\,\Delta \tau$$

where F_v is tendency of v due to backscatter forcing. The change in v during one CA step (Δv) is given by:

$$\Delta v = F_v\,\Delta \tau = \frac{1}{2}\alpha\,\Delta s \frac{\partial \Psi}{\partial x}\sqrt{\hat{D}\,\Delta \tau} = \frac{1}{2}\alpha\,\Delta\Psi\sqrt{\hat{D}\,\Delta \tau}$$

where $\Delta\Psi$ is the change of Ψ over distance Δs. Denoting the ensemble average by angle brackets, the mean square velocity change is

$$<(\Delta v)^2> = \frac{1}{4}\alpha^2 <(\Delta\Psi)^2>\hat{D}\,\Delta \tau$$

and with an identical contribution from backscatter acceleration in the y direction it follows that the rate of kinetic energy input (ε_b) is given by:

$$\varepsilon_b = \frac{<(\Delta u)^2> + <(\Delta v)^2>}{2\Delta \tau} = \frac{1}{4}\alpha^2 <(\Delta\Psi)^2>\hat{D}.$$

For a particular choice of pattern generation algorithm $<(\Delta\Psi)^2>$ is fixed and the backscatter fraction $\varepsilon_b / \hat{D}$ is a function of α alone i.e.

$$\frac{\varepsilon_b}{\hat{D}} = \frac{1}{4}\alpha^2 <(\Delta\Psi)^2> \tag{3}$$

Horizontal diffusion and smoothing due to interpolation also affect the temperature field. The corresponding rate of loss of available potential energy (APE) is crudely estimated using a quasi-geostrophic definition i.e.

$$APE = \frac{g}{2B_0(z)}\left(\frac{T'}{T_0}\right)^2 \tag{4}$$

where T' is the departure of the temperature from a height-dependent basic state value $T_0(z)$ and $B_0(z)$ is the static stability. For convenience it is effectively assumed that

$$B_0(z) = B_0(0)\left(\frac{T_0(0)}{T_0(z)}\right)^2$$

so that eq. (4) becomes

$$APE = \frac{g}{2B_0(0)T_0(0)^2} \cdot T'^2 \tag{5}$$

with $B_0(0) = 1 \times 10^{-5} m^{-1}$ and $T_0(0)=300$ K.

In the forecast model, T' is computed by removing spectral contributions with $n \leq 2$ from the spherical harmonic expansion of potential temperature. The APE tendency is then determined by multiplying the gridpoint temperature tendency associated with horizontal diffusion by $g\ T'/(B_0(0)T_0(0)^2)$. Given the considerable uncertainty associated with the fraction of energy backscattered, the inaccuracy of this quasi-geostrophic definition of APE is not an overriding concern. The APE tendency is included in the total dissipation variable D with the tacit assumption that only kinetic energy will be backscattered. Averaged over a sufficiently large area the diffusive contribution to the energy will be negative representing a drain of energy from the resolved flow. D_N is minus this value and represents the rate of increase of sub-grid scale kinetic + available potential energy energy.

To account for the effects of semi-Lagrangian interpolation error, D_N is multiplied by a certain factor determined from a simple offline calculation. This involves computing the loss of kinetic energy in a poorly-resolved idealized vortex resulting from the separate application of bi-harmonic diffusion and the forecast model's interpolation scheme. The dissipation rates associated with these two effects are of the same order of magnitude : if they were not, horizontal diffusion would either be far too large and spoil the accuracy of near-grid scale advection or would be too small to be worth including. The factor used here (based on the offline calculations) is 3, implying that the diffusive influence of interpolation to the departure point is stronger by a factor of two than bi-harmonic diffusion itself.

D_{GW} is computed within the operational forecast model by estimating the change in kinetic energy due to mountain drag alone. The implementation of gravity wave and mountain flow blocking drag in the ECMWF forecast model assumes that this energy is permanently lost from the flow and dissipated as heat so a matching thermal increment is added to the temperature field. To be consistent with the transfer of kinetic energy back to the resolved scales the thermal increment should be reduced accordingly. This effect has been overlooked here but is not thought that the impact will be significant.

The evaluation of D_C is composed of two terms; one associated with the work done on the resolved flow by the force associated with convective momentum transport and the other is due to the kinetic energy exported into the cloud environment by detrainment. The former term is evaluated in the same way as for gravity wave drag. The other detrainment term is conveniently evaluated by multiplying the convective parametrization scheme's mass detrainment rate at any height by a locally diagnosed updraught kinetic energy (Tiedtke, 1989). This is obtained from the scheme's energy budget equation involving buoyancy production, entrainment and detrainment. Eq.(2) is evaluated on all levels in gridpoint space and then spectrally-transformed so that the vorticity tendency can be computed by multiplying the resulting spectral coefficients by $-n(n+1)/a^2$. Vorticity increments are then computed from the tendencies and added to the spectral vorticity amplitudes alongside the spectral horizontal diffusion increments.

4. Impact on the ECMWF forecast model

4.1 Kinetic energy dissipation rate contributions

In the absence of a theory for the backscatter ratio $\varepsilon_b / \hat{D}$ the constant α in eq.(2) should be tuned so as to maximize its positive effect on measures of EPS forecast skill such as the rank probability skill score. Here α is set to unity and Δs is the gridlength at the equator of the 2-degree grid.

For physical consistency the backscatter rate must not exceed the computed total energy dissipation rate (strictly, the energy drain rate). Before considering such matters it is instructive to look at the spatial distribution of the total dissipation rate and its decomposition into the contributions described in the last section. The total smoothed dissipation rate at T+24 hrs (verifying at 12Z on October 16 2000) is given in Figure 3(a). Globally averaged this term, which represents a rate of production of sub-gridscale kinetic energy, is comparable in size with the rate of dissipation of energy in parametrized turbulent mixing (i.e. 2.87).

The contribution of numerical dissipation (Figure 3b) is at its greatest in storm track regions (e.g. off the east coasts of the USA and over some of the main mountainous zones (e.g. Andes and Himalayas) though with typical values less than 10 . The mountain drag contribution (Figure 3c) has huge local peaks in the dissipation rate with values as high as 200 in the Andes.

Spectral smoothing causes these to appear as circular regions extending over the sea in places. Although the energy dissipation rate due to mountain drag is locally very large its global mean contribution is less than 10% of the total.

Finally, the contribution of deep convection to the sub-gridscale kinetic energy is, as one would expect, concentrated in the tropics (Figure 3(d)). Locally the kinetic energy production rate is ~20 Wm^{-2} and its global-mean is comparable with the estimate of numerical dissipation at 1.27 Wm^{-2}. Of course there is a fair amount of uncertainty in the magnitude of these dissipation rates (kinetic energy production rates in the case of convection) but since the backscatter fraction is not known, this need not concern us at this stage. On the other hand it is important to make sure that the actual rate of transfer of kinetic energy back to the resolved scales is less than the computed dissipation rate. The global rate of energy backscatter (E_b) is given by:

$$E_b = -\iiint \varsigma F_\psi a \cos\phi \; dp \, d\phi d\lambda \tag{6}$$

where ς is the vertical component of vorticity, a is the Earth's radius, ϕ is latitude, λ is longitude and p is pressure. E_b was evaluated as a mean over the entire 10-day forecast (comprising 20 half-daily model dumps) and found to be ~0.67 Wm^{-2} i.e. about one quarter of the global dissipation rate at T+24 hrs. The equivalent 10-day average global-mean dissipation rate was found to ~ 3.0 Wm^{-2} which is about 22 % of the total dissipation rate.
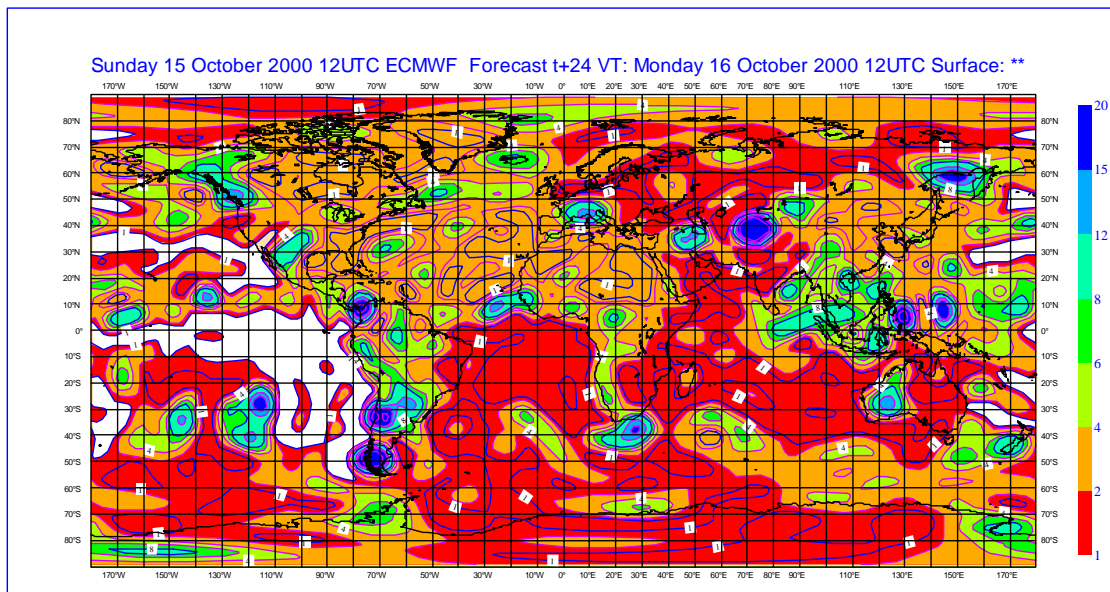
Figure 3(a) Total smoothed 'dissipation rate' comprising contributions from horizontal diffusion (augmented to account for semi-Lagrangian interpolation error), gravity wave/mountain drag and deep convection. The global-mean dissipation rate = 2.87Wm^{-2} .
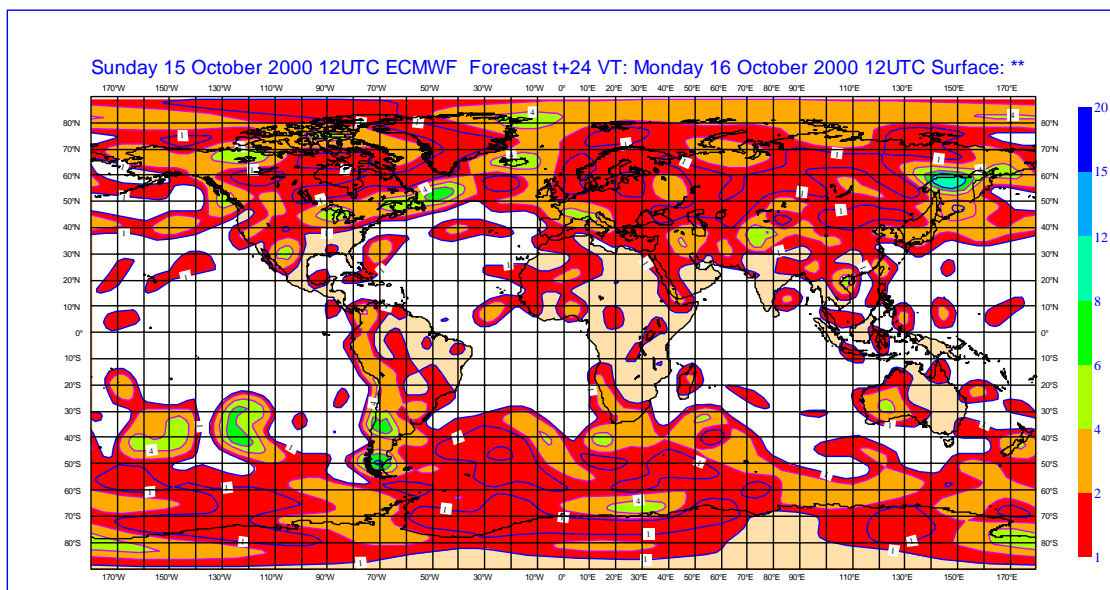

Figure 3(b) Smoothed numerical contribution to the total depth-integrated energy dissipation rate (Wm^{-2}). Global-mean= 1.21Wm^{-2} .
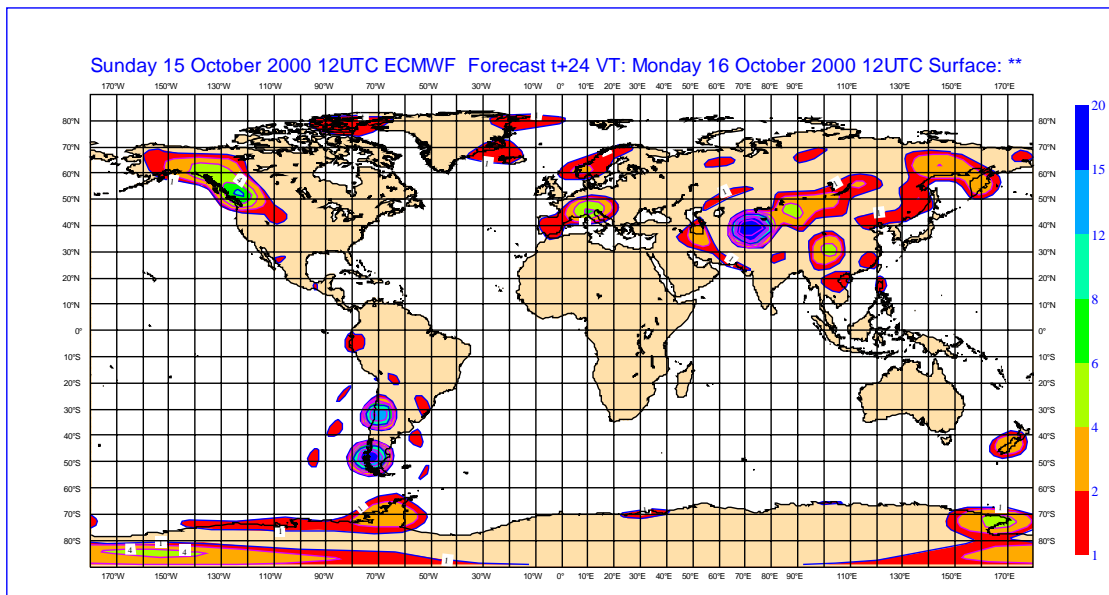
Figure 3(c) Smoothed gravity wave and mountain drag contribution to the depth-integrated total energy dissipation rate (Wm^{-2}). Global-mean=0.26Wm^{-2}
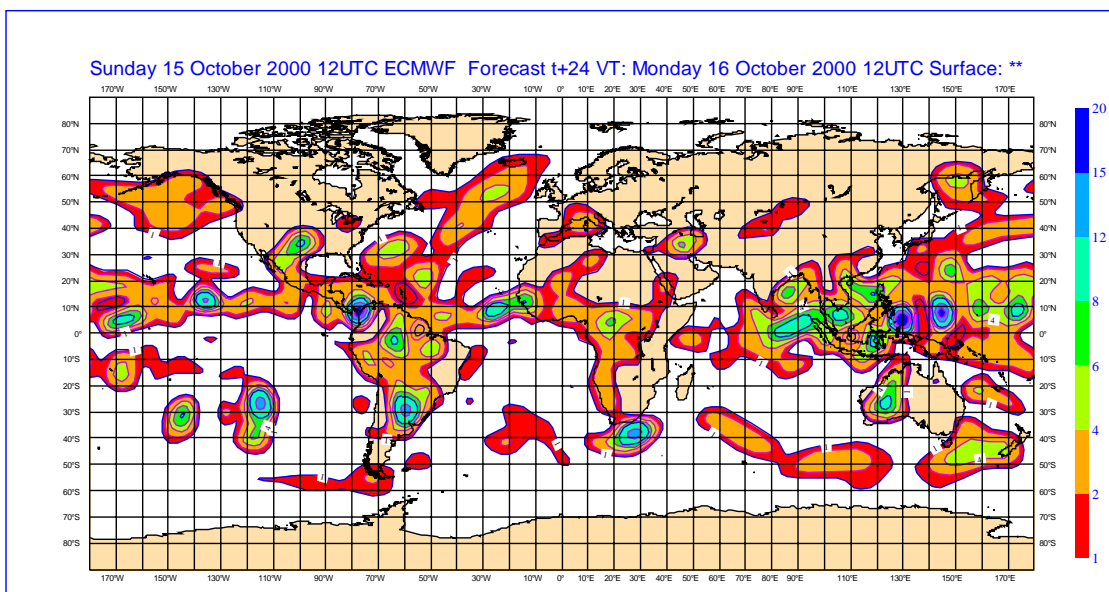
Figure 3(d) Smoothed convective contribution to the depth-integrated kinetic energy source(Wm^{-2}) Global-mean=1.27Wm^{-2}.

The streamfunction forcing field at two model levels is shown in Figure 4(a) and (b). At model level 47 (approximately 1.7 km above the surface) the streamfunction forcing is fairly uniformly distributed over the global whereas at level 31 (~10.4 km) the forcing tends to dominate in the tropics where convective mass detrainment is large. The effect of backscatter on the energy spectrum can be seen in Figure 5 where the kinetic energy density is plotted against spherical harmonic order at T+240 hr for runs with and without the streamfunction forcing. The control run (without backscatter) exhibits a known deficiency of the ECMWF forecast model - the absence of a small spectral slope (approximating $k^{-5/3}$) at the smallest resolvable scales. At a spectral truncation of T159 it could be argued that there is insufficient resolution to capture the observed

transition from k^{-3} to $k^{-5/3}$ spectral slope. However runs at T799 also show no sign of the $k^{-5/3}$ spectral slope either (Figure 6). With the backscatter scheme there is substantially more energy at smaller scales (Figure 7) and it could be argued that we are compensating for a model deficiency by injecting energy at the smallest resolvable scales.
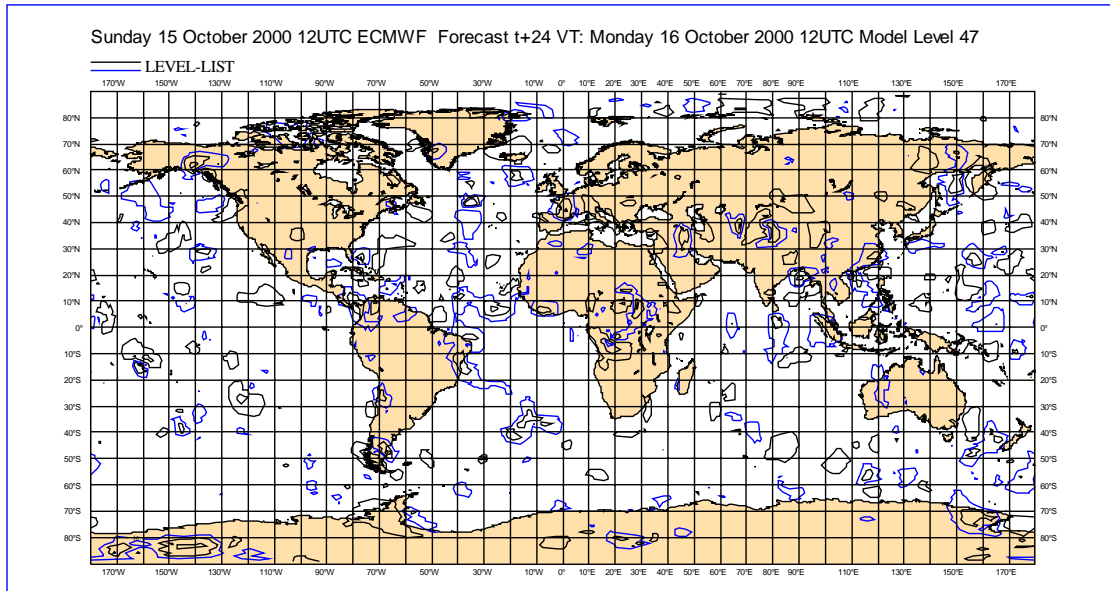

Figure 4(a) Streamfunction forcing pattern (F_ψ) at level 47 (~ 1.7 km). Contour interval: $16m^2s^{-2}$. blue contour has the value $16m^2s^{-2}$
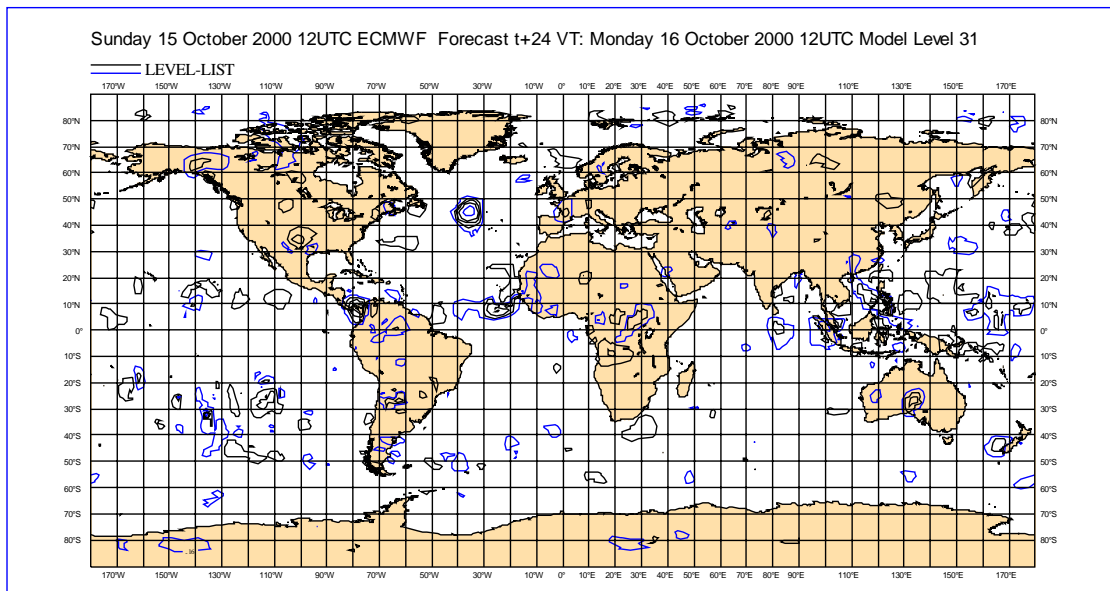
Figure 4(b) Streamfunction forcing pattern at level 31 (~ 10.4 km Contour interval: $16m^2s^{-2}$. blue contour has the value $16m^2s^{-2}$
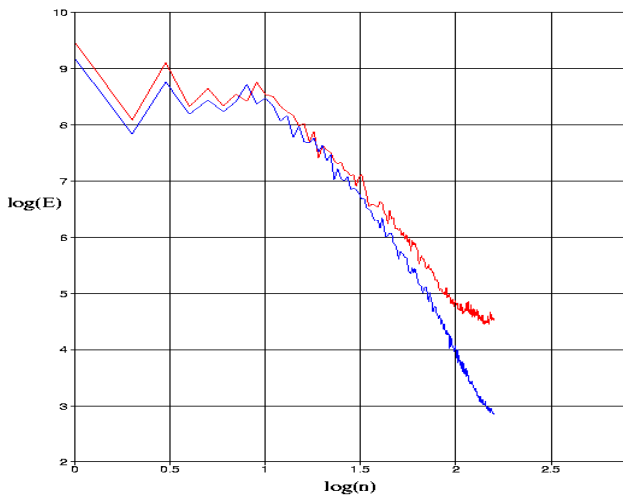
Figure 5 Kinetic energy spectra at T+240 in T159 control run (red) and with backscatter (blue). E has units of $m^3 s^{-2}$ and n is the spherical harmonic order.
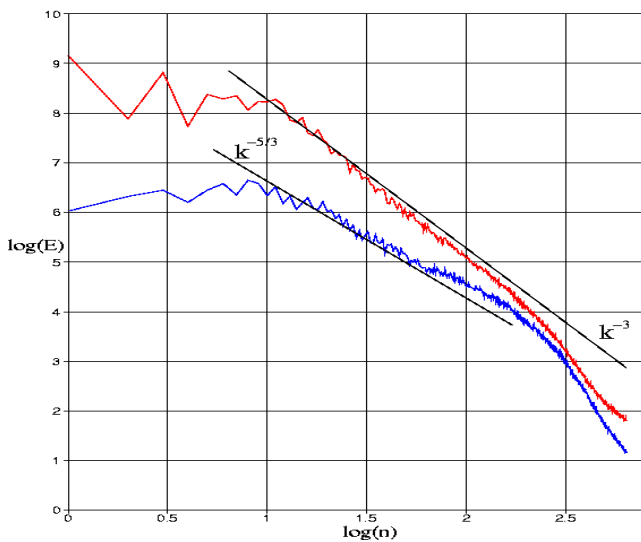

Figure 6 Energy spectra at day 10 of a forecast with T799 resolution. The red curve is the total kinetic energy spectrum of the horizontal wind and the blue curve is the contribution associated with the divergent wind. The solid black lines depict the inertial sub-range spectral slopes of $k^{-5/3}$ and k^{-3}. The energy density in scales for which $n > 200$ falls away from the corresponding constant slope line.
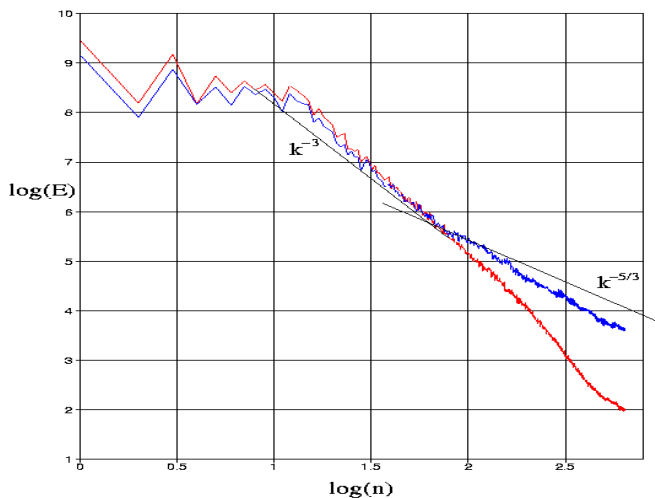

Figure 7 Energy spectra at day 5 in forecasts run at T799: with stochastic backscatter (blue curve) and without backscatter (red curve). log(E) is the logarithm (base 10) of the energy density and n is the spherical harmonic order.

It is interesting that the energy in the divergent part of the horizontal wind *does* appear to approximately follow a $k^{-5/3}$ spectral slope. One possible interpretation of the observed $k^{-5/3}$ spectrum is that the model's divergent wind energy is suppressed at short wavelengths and the $k^{-5/3}$ spectral slope should extend to the smallest resolvable wavelength. This seems a compelling argument but is not what we are seeing in Figure 7 since it is energy in the rotational component of the horizontal wind that dominates the spectrum for *n > 200*.

Tung and Orlando (2003) argue that the mesoscale $k^{-5/3}$ spectrum can be explained within the context of quasi-geostrophic theory (i.e. without gravity wave contributions) as a weak energy cascade to small scales. They used a highly scale-selective hyperviscosity (∇^{20}) that was tuned to give a very small dissipation rate (i.e. ~ $10^{-6} m^2 s^{-3}$ which about $0.01 W m^{-2}$). One interpretation of the more realistic mesoscale energy spectrum in their model compared with the ECMWF forecast model is that their model better matches the real kinetic energy dissipation rate in the free troposphere. Such small dissipation rates probably cannot be achieved in the current generation of NWP models in which frontogenesis and scale collapse is more realistically described than in the quasi-geostrophic system.

4.2   Effect on skill and spread in EPS experiments

In order to quantify the effect of the CASBS scheme sets of 10 EPS forecasts have been made for the cases

  i)   initial perturbations only

  ii)   operational stochastic physics

  iii)   CASBS (i.e. backscatter)

Forecasts beginning from 12Z on October 15 2000; November 10, 15 and 20; December 10, 15 and 20 of 2003 together with January 9, 14 and 19 of 2004 are labelled Set A and those beginning from 12Z on June 5, 10, 15 and 20; July 10,15 and 20 together with August 9, 14 and 19 of 2003 are labelled Set B. All forecasts were run for 10 days at T159 spectral truncation with 60 vertical levels and one-hour time steps. Each forecast ensemble comprises 51 members made up of one unperturbed control forecast and 50 member forecasts generated from perturbed initial conditions. Each perturbed forecast with operational stochastic physics has a different set of random numbers to use as multipliers of the model's physical parametrization tendency vector (each physical tendency has a different random number also). In the CASBS runs the CA was 'spun up' from a different random seeding of the initial state but thereafter not reliant upon a random number generator. In this sense the CA evolution is deterministic for each forecast member.

The impact of CASBS and operational stochastic physics is characterized by statistical properties such as the root-mean squared spread about the control forecast and standard probabilistic measures of skill such as the Brier score, the ROC area and Rank Probability Score (RPS) e.g. Jolliffe and Stephenson (2003). Attention will be confined to the 500-hPa height field (Z_{500}) and scoring computed with respect to events with binary outcomes defined by

$$Z_{500} - Z_{500}^{c\,\lim} > T_j \tag{7}a$$

where $Z_{500}^{c\,\lim}$ is the climatalogical-mean 500 hPa height field and T_j is a set of positive threshold values or

$$Z_{500} - Z_{500}^{c\,\lim} < -T_j \tag{7}b$$

for negative height anomaly events.

Figure 8(a) and (b) show the spread for ensemble forecast set A over the forecast period, together with the mean error of the control runs, for the northern and southern hemispheres respectively. In both figures the operational stochastic physics can be seen to increase the spread by a small amount though not as much as the CASBS . Good performance of the ensemble forecast system requires that the increase in spread approximately matches the growth of forecast error in the control run. Beyond day 4 or 5 stochastic backscatter is certainly increasing the spread favourably though for shorter forecast ranges the spread is excessive. In general the spread and control forecast error growth is quite similar in the two hemispheres.
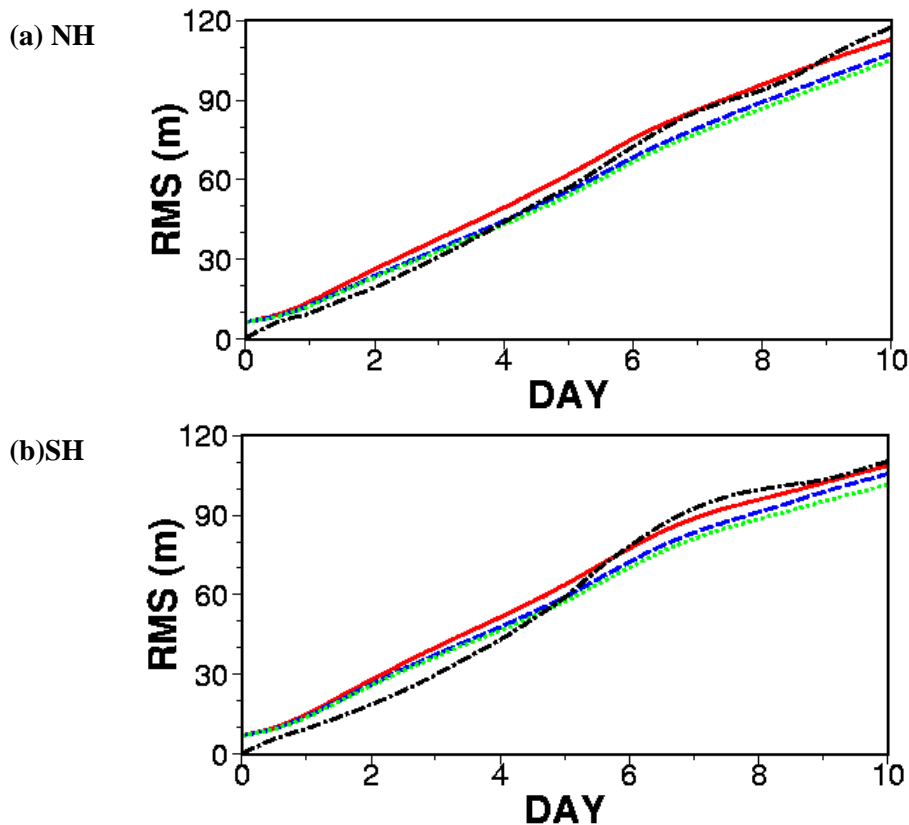

Figure 8 Spread (defined as the ensemble-average of the root-mean-square differences between perturbed member forecasts and the control forecast) for Set A (a) northern hemisphere (b) southern hemisphere. The ensemble forecasts with initial perturbations only are given by the dotted green curve; with operational stochastic physics are given by the dashed blue curve and with CASBS given in red. The black dot-dash curve is the mean error of the 10 control forecasts defined by the differences between forecasts and their corresponding verifying analyses.

Figure 9(a) and (b) show the time evolution of the Rank Probability Skill Score (RPSS) based on 10 thresholds for the northern and southern hemispheres respectively. The RPSS has the advantage of effectively integrating the Brier score over many event thresholds and so reduces the amount of information required to assess skill (as does integrating over hemispheres). In Figure 9(a) after day 4 it is clear that the CASBS runs have somewhat higher skill than those of the operational stochastic physics although the differences made by either scheme are not large. In the southern hemisphere, skill improvement in the CASBS runs appears after day 6. On a cautionary note one must assume that wobbles in the curves are a sign that the sample size is still too small. The relative spacing of dips in the curves between day 6 and 9 of Figure 9(b) may not therefore be representative. The small overall improvements of skill later in the forecast probably follow from a better match between spread and control forecast error using CASBS (Figure 8). The

over-forecasting of spread before day 4 makes a small negative impact in skill although barely visible in Figure 9(a).
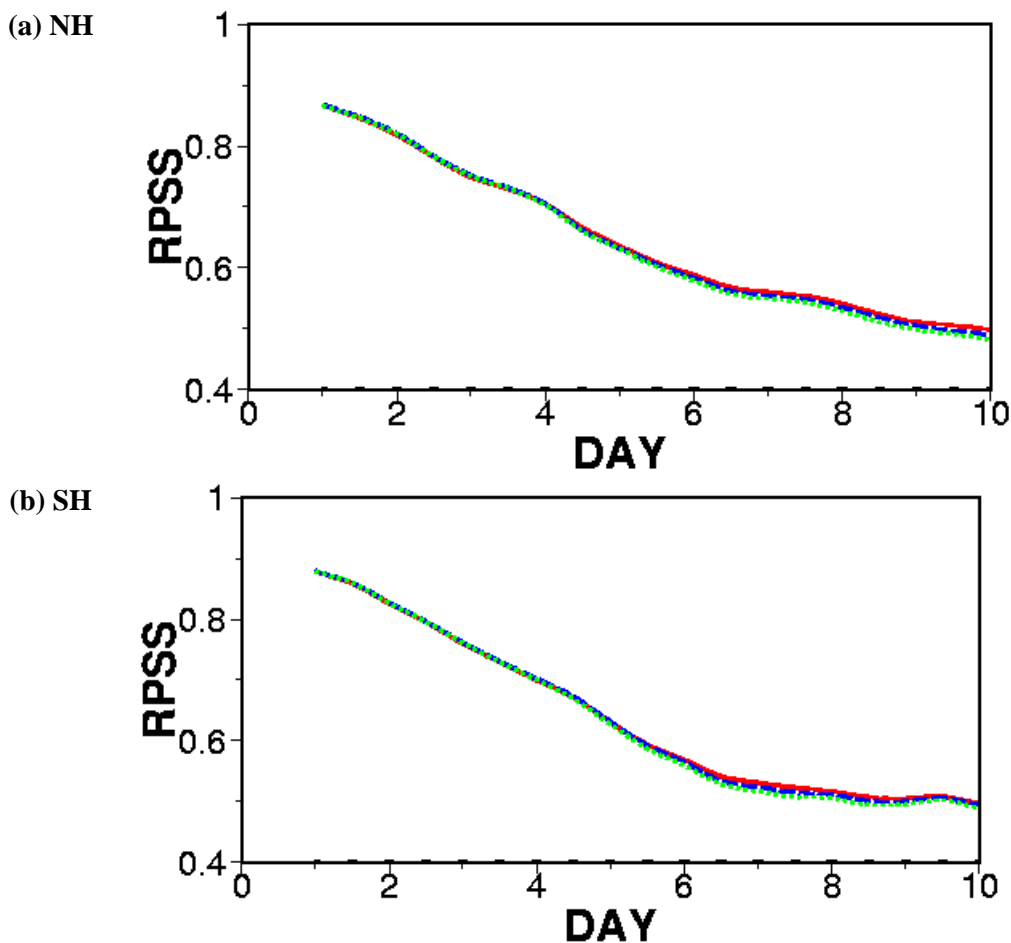
(a) NH

(b) SH

Figure 9 Rank Probability Skill Score (RPSS) averaged over 10 EPS forecasts (set A) for (a) northern hemisphere, (b) southern hemisphere.(curve colours and style as in Figure 8).

Another popular analysis tool for evaluating the skill of a forecasting system is the Relative Operating Characteristic (ROC), which is a graph of hit rate versus false alarm rate plotted for a range of different decision thresholds (Jolliffe and Stephenson, 2003). Both hit rate and false alarm rate are defined on the range 0 to 1 and the area under the curve (the ROC area) is a measure of skill with 1 being the maximum and ½ corresponding to zero skill. Figure 10(a)-(e) show global ROC area plots (for set A) versus forecast time for different 'events' of the form given by inequalities (7a) and (7b). In most cases during the first 6 days of the forecast CASBS gives a small but consistent improvement in the ROC area over the operational stochastic physics and initial-perturbations-only forecasts. Thereafter the performance of the CASBS forecasts is at least competitive with the stochastic physics scheme and does very well indeed for m, which might be regarded as a test for blocking a certain geographical locations like the European sector. Only the case m has lower skill than the stochastic physics runs (and also the case which is not shown here).

The rank probability skill scores for northern and southern hemispheres in forecast set B (10 forecasts from June, July and August cases) are shown in Figure 11(a) and (b). The impact of backscatter in the northern hemisphere is less good, particularly in the first four days where skill is degraded with respect to the initial-

perturbations only forecast. Nevertheless the southern hemisphere RPSS shows some superiority over the operational stochastic physics runs - similar to the skill of the set A forecasts. The reason for the degradation of the northern hemisphere summer forecasts is not known currently but may be related to excessive tropical cyclone formation. It is probably significant that the northern hemisphere summer has the weakest zonal circulation out of the four combinations of hemisphere and season, which may imply that the backscatter forcing is too strong relative to the flow strength.

The root-mean square forecast member spread plotted for each hemisphere in Figure 12 shows how the match of EPS spread to control forecast error growth relates to skill. In the northern hemisphere CASBS provides much more additional spread than operational stochastic physics and this causes the spread to significantly exceed the control forecast error. In fact in these forecasts there doesn't seem to be a requirement for any additional EPS forecast spread beyond what is obtained from the initial perturbations. In the southern hemisphere a very good match between EPS spread and control forecast error is obtained after day 4 consistent with the good RPSS seen after day 6.

The global ROC area for set B is shown in Figure 13 for the same decision thresholds as for set A (Figure 10). Overall the performance of CASBS relative to the operational stochastic physics scheme is quite similar to that found in set B with positive geopotential height anomaly events scoring much better than negative. These global mean scores hide the poor performance in the northern hemisphere as can be seen in Figure 14 which gives ROC area for the event $Z_{500} - Z_{500}^{c\,\mathrm{lim}} > -100$ m. After day 4 the ROC score falls below that for the initial-perturbations-only runs indicating a definite problem with over-forecasting cyclone strength.

It is also interesting to note how consistent the operational stochastic physics is in providing small improvements to the ROC area at all forecast times.
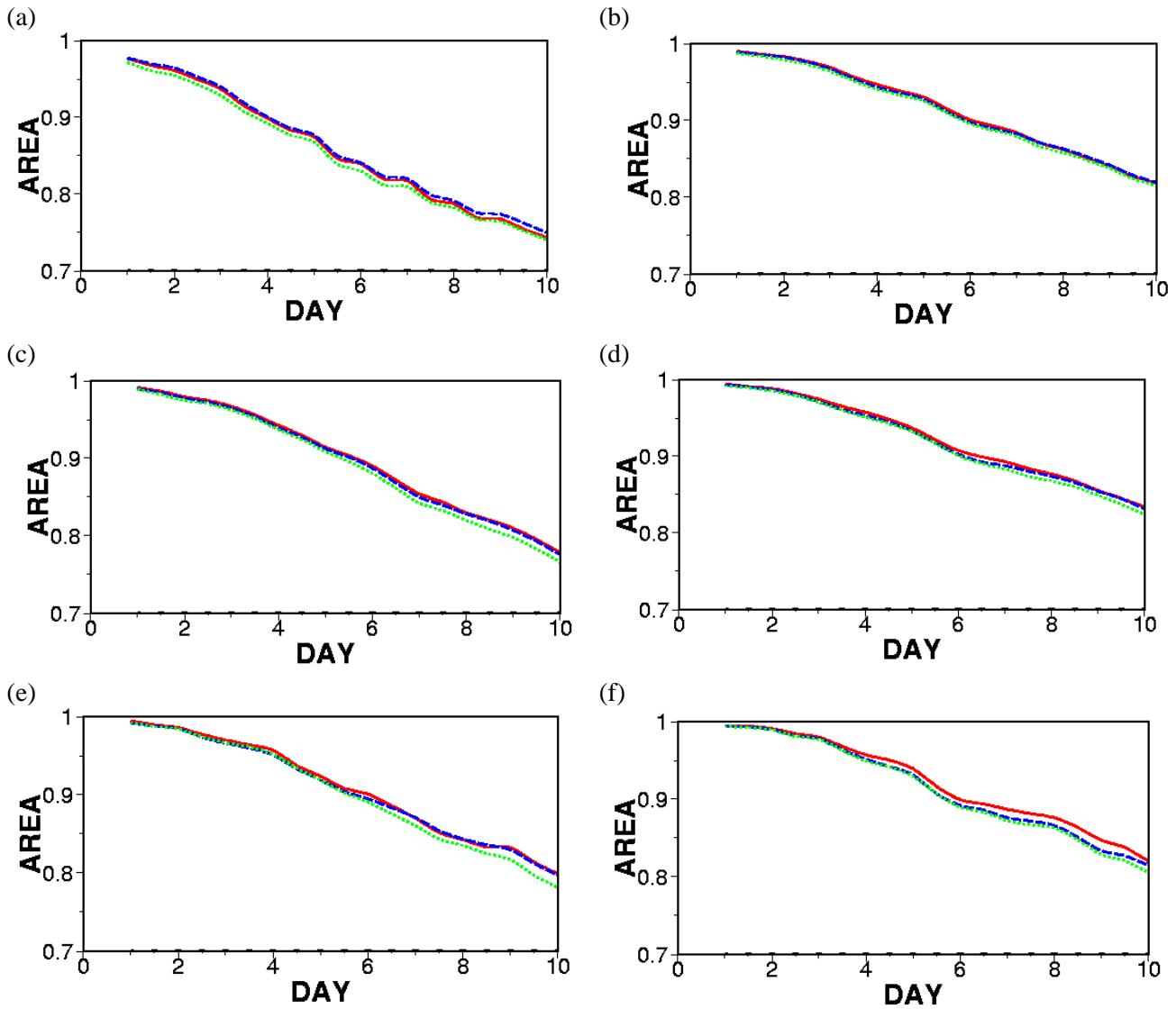
(a)

(b)

(c)

(d)

(e)

(f)

Figure 10 Mean over 10 forecasts (set A) of the global ROC area defined for 6 event thresholds involving the 500 hPa geopotential height field anomaly , (a) $Z_{500} - Z_{500}^{c\,\lim} < -25\,m$; (b) $Z_{500} - Z_{500}^{c\,\lim} < 25\,m$; (c) $Z_{500} - Z_{500}^{c\,\lim} < -50\,m$; (d) $Z_{500} - Z_{500}^{c\,\lim} < 50\,m$; (e) $Z_{500} - Z_{500}^{c\,\lim} < -100\,m$ and (f) $Z_{500} - Z_{500}^{c\,\lim} < 100\,m$. The plotted curves are for CASBS (red), stochastic physics (dashed blue) and initial perturbations only (dotted green).
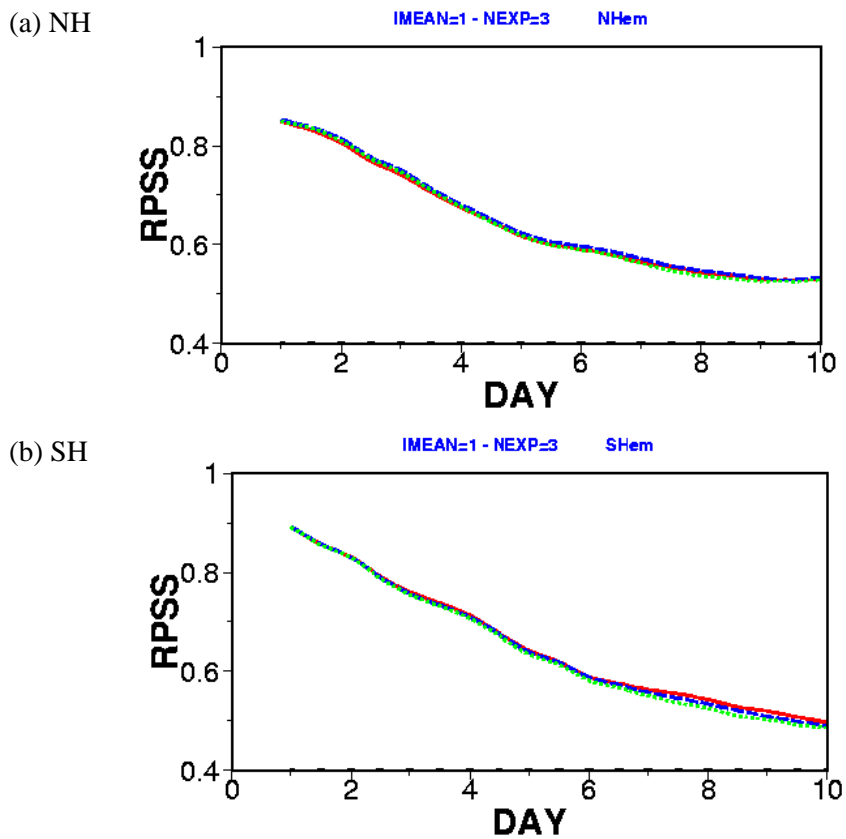
(a) NH

IMEAN=1 - NEXP=3   NHem

(b) SH

IMEAN=1 - NEXP=3   SHem

Figure 11 Rank Probability Skill Score (RPSS) averaged over 10 EPS forecasts (set B) for (a) northern hemisphere, (b) southern hemisphere.
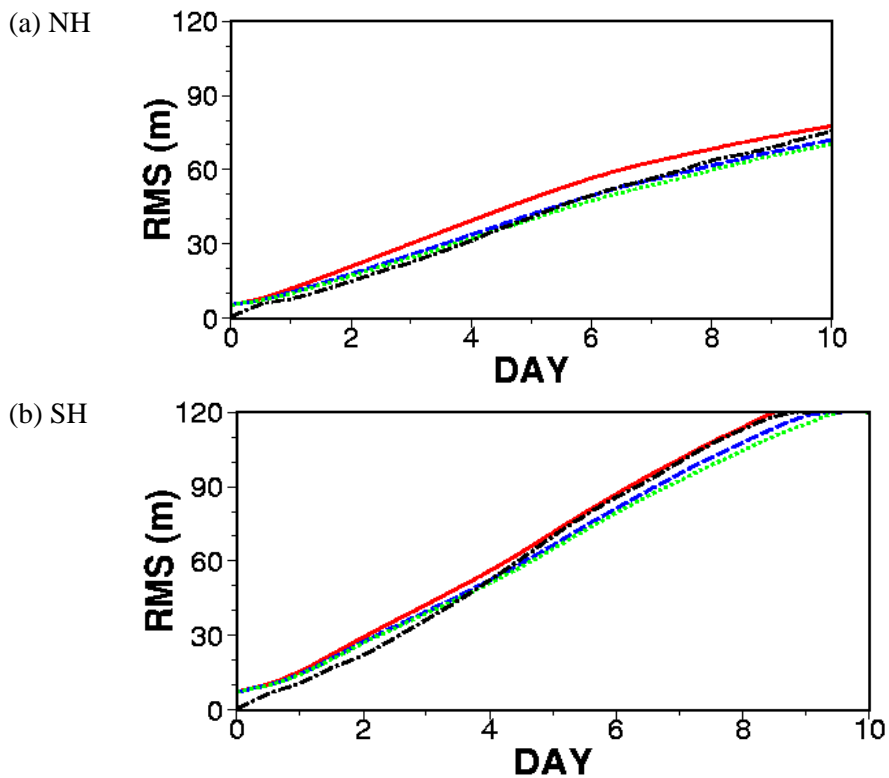
(a) NH

(b) SH

Figure 12 EPS spread (as in Figure 8 except for forecast set B).
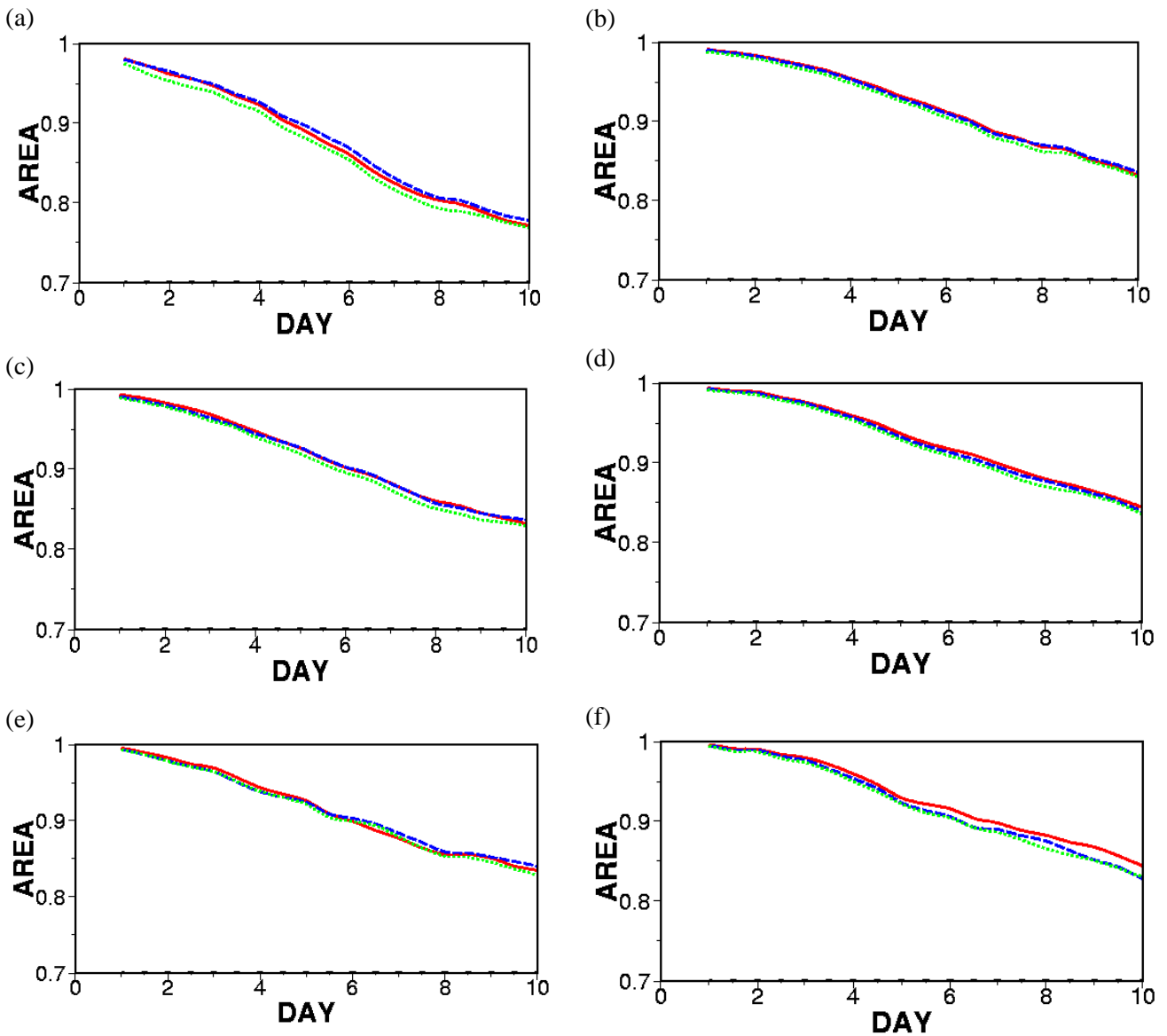
Figure 13 Mean over 10 forecasts (set B) of the global ROC area defined for 6 event thresholds involving the 500 hPa geopotential height field anomaly (as for Figure 10)
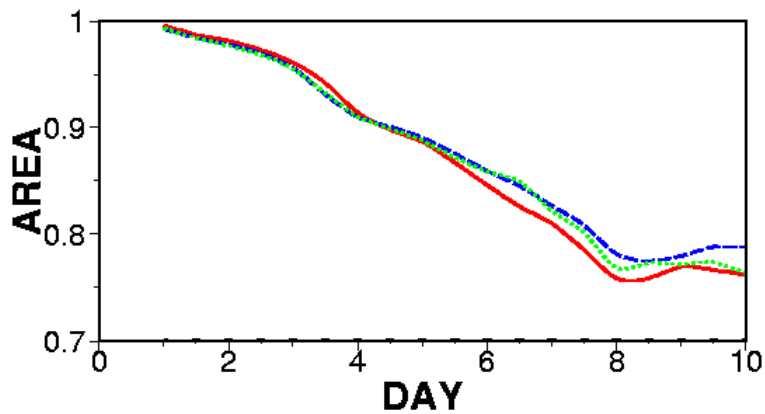

Figure 14 ROC area based on $Z_{500} - Z_{500}^{c\,\mathrm{lim}} < -100\,m$ for the northern hemisphere in the set B forecasts

5.   Conclusion

A physical argument has been put forward for the introduction of kinetic energy sources terms into NWP models that counteract the numerical and parametrized energy drain occurring in the near-grid scale. In this respect the approach taken here has similar motivation to stochastic energy backscatter used in large eddy simulation of boundary layer turbulence. In addition to offsetting the energy drain, a contribution to the net kinetic energy source is also assumed to arise from deep convection wherein a certain fraction of the kinetic energy released by buoyancy forces is assumed to be injected back onto the partially resolved scales of a forecast model. The kinetic energy contributions from these distinct numerical and physical sources is summed as a parameter called the 'total dissipation rate'.

A numerical implementation of these ideas as been developed and tested in the ECMWF forecast model energy. Kinetic energy is backscattered by introducing vorticity perturbations into the flow with a magnitude proportional to the square root of the total dissipation rate. The spatial form of the vorticity perturbations is derived in part from a cellular automaton that crudely represents the spatial and temporal correlations of the atmospheric mesoscale. The CA is an experimental aspect of the scheme which could provide the basis for a more intelligent two-way coupled approach in which the spatial scale of the patterns could be functionally related to the model flow. In the form used here the CA is nothing more than an exotic pattern generator and no justification for its superiority to any other algorithm (e.g. smoothed random number fields) has been given. Further investigation into its properties and indeed other forms of CA would be desirable, particularly in a more idealized modelling context.

The scheme, CASBS, is an effective means of generating EPS spread associated with model error. In the cases shown here where the member spread about the control matches the error of the control (unperturbed) forecast the skill of the EPS forecast is good. Because the operational stochastic physics scheme only generates a small amount of additional spread, its impact on skill is small but consistently positive. CASBS has been tuned to provide a larger spread and although its impact on 500 hPa skill is more sensitive to the event being forecast than the operational stochastic physics scheme, these first results look encouraging. For the backscatter ratio used here (~25 %) the global rank probability skill score is somewhat better using CASBS than the operational scheme - except for the northern hemisphere summer where the spread generated is excessive.

On a practical level one should note that the computational demands of testing variants of the scheme is high given the large number of forecasts required for statistical reliability. It is hoped that further refinements of CASBS will lead to more consistent and robust performance without some of the known negative side-effects of the present operational scheme (e.g. excessive frequency of high precipitation events). Outstanding issues to address include the vertical structure of the streamfunction forcing, the relative contribution of the different dissipation terms and the statistical properties of the cellular automaton. Separate process studies (e.g. with cloud-resolving models) will help to calibrate the energy backscatter ratios and provide statistical information relating to the desired spatial and temporal correlation of the streamfunction forcing.

discussions. In particular, Peter Janssen alerted me to the deficiencies of the ECMWF model energy spectrum.

References

Blumen, W. (1990) A semi-geostrophic Eady-wave frontal model incorporating momentum diffusion. Part II: Kinetic energy and enstrophy dissipation. *J. Atmos. Sci.*, 47, 2903-2908.

Buizza,R., Miller,M. and Palmer, T.N. (1999) Stochastic representation of model uncertainty in the ECMWF Ensemble Prediction System. *Q.J.R. Meteorol. Soc.,* 125, 2887-2908.

Chapman, D. and Browning, K.A. (2001) Measurements of dissipation rate in frontal zones. *Q.J.R. Meteorol. Soc.,*127, 1939-1959.

Côte, J. and Staniforth, A. (1988) A two-time-level semi-Lagrangian semi-implicit scheme for spectral models. *Mon. Wea. Rev.*, 116, 2003-2012.

Cullen, M.J.P. and Purser, R.J. (1984) An extended theory of semi-geostrophic frontogenesis. *J. Atmos. Sci.*, 41, 1477-1497.

Fjortoft, R. (1953) On the changes in the spectral distribution of kinetic energy for a two-dimensional non-divergent flow. *Tellus*, 5, 225.

Gardener M. (1970) The fantastic combinations of John Conway's Game of Life. *Scientific American*, 23, 120-123.

Jolliffe, I.T. and Stephenson, D.B. (Eds.) (2003) Forecast verification : A Practitioner's Guide in Atmospheric Science. *John Wiley and Sons Ltd,* Chichester, England. 240 pp.

Kennedy P.J. and Shapiro M.A. (1975) The energy budget in a clear air turbulence zone as observed by aircraft. *Mon. Wea. Rev.*, 103, 650-654.

Lilly, D.K. (1983) Stratified turbulence and the mesoscale variability of the atmosphere. *J. Atmos. Sci.*, 40, 749-761.

Lin, J.W-B. and Neelin, J.D. (2000) Influence of a stochastic moist convective parametrization on tropical climate variability. *Geophys. Res. Lett.*, 27, 3691-3694.

Lin, J.W-B. and Neelin, J.D. (2002) Considerations for stochastic convective parametrization. *J. Atmos. Sci.,* 59, 959-975.

MacVean, M.(1983) The effects of horizontal diffusion on baroclinic development in a spectral model. *Q.J.R. Meteorol. Soc.*, 109, 771-783.

Mason, P.J. and Thomson, D.J. (1992) Stochastic backscatter in large-eddy simulations of boundary layers. *J.Fluid Mech.*, 242, 51-78.

McCaplin, J.D. (1988) A quantitative analysis of the dissipation inherent in semi-Lagrangian advection. *Mon. Wea. Rev*., 116, 2330-2336.

Nastrom, G.D. and Gage, K.S. (1985) A climatology of atmospheric wavenumber spectra of wind and temperature observed by commercial aircraft. *J. Atmos. Sci*., 42, 950-960.

Palmer, T.N. (1997) On parametrizing scales that are only somewhat smaller than the smallest resolved scales, with application to convection and orography. *Workshop on New Insights and Approaches to Convective Parametrization. 4-7 November 1996. ECMWF, Reading, UK.*

Ritchie, H. (1988) Application of the semi-Lagrangian method to a spectral model of the shallow-water equations. *Mon. Wea. Rev*., 116, 1587-1598.

Shutts, G.J. and Gray, M.E.B. (1994) A numerical modelling study of the geostrophic adjustment process following deep convection. *Q.J.R. Meteorol. Soc*., 120, 1145-1178.

Simmons, A. and Hoskins, B.J. (1978) The life cycles of some nonlinear baroclinic waves. *J. Atmos. Sci*., 35, 414-432.

Tiedke, M. (1989) A comprehensive mass flux scheme for cumulus parametrization in large scale models. *Mon. Wea. Rev.*, 117, 1779-1800.

Stephenson, D.B.(1994) The impact of changing the horizontal diffusion scheme on the northern winter climatology of a general circulation model. *Q.J.R. Meteorol. Soc*., 120, 211-226.

Tung , K-K.and Orlando, W.W. (2003) The k^{-3} and $k^{-5/3}$ energy spectrum of atmospheric turbulence: quasi-geostrophic two-level model simulation. *J. Atmos. Sci.*, 60, 824-835.

Vallis, G.K., Shutts, G.J. and Gray, M.E.B. (1997) *Q.J.R. Meteorol. Soc*., 123, 1621-1652.

Williams, P.D. (2003) Nonlinear interactions of fast and slow modes in rotating stratified fluid flows. *PhD Thesis,* Oxford University, England.

Williams, P.D.,Haine,T.W.N. and Read, P.L.(2004) Stochastic resonance in a nonlinear model of a rotating, stratified shear flow, with a simple stochastic, inertia-gravity wave parametrization. *Nonlinear Processes in Geophysics*, 11, 127-135.

Wolfram, S. (2002) A New Kind of Science. *Wolfram Media, Inc*.